Supplementary information

Electrode binder design for high-power, low-Pt loading and durable high temperature fuel cells

Hui Li,[a] Peipei Zuo,[a] Wenyi Wu,[a] Gonggen Tang,[a] Junkai Fang,[a] Tongwen Xu[a] and Zhengjin Yang*[a]

[a] Key Laboratory of Precision and Intelligent Chemistry, Department of Applied Chemistry, School of Chemistry and Materials Science, University of Science and Technology of China, Hefei, 230026, P. R. China, Email: yangzj09@ustc.edu.cn (Z. Yang)

This PDF file includes:

Supplementary Figures 1 to 34, Supplementary Table 1-5

Experimental

Materials. Bisphenol A (BP-A, 98%), methane sulfonic acid (MEA, 98%), dimethyl sulfate (DMS, 99%), trifluoromethanesulfonic acid (TFSA, 99%), and p-terphenyl (TP, 99%) were purchased from Energy Chemical Co. Ltd (Shanghai). Pentafluorobenzaldehyde (PFBA, 98%) and tris(trimethylsilyl) phosphite (TSP, 95.0%) were acquired from TCI Development Co., Ltd (Shanghai). Methylene chloride (DCM), N-methyl pyrrolidone (NMP), dimethyl sulfoxide (DMSO), hydrochloric acid (HCl, 37%) and potassium carbonate (K_2CO_3) were provided by Sinopharm Group Chemical Reagent. Pt/C catalyst (60 wt% Pt, HISPEC 9100, Johnson Matthey), carbon paper (TGP-H-060, TORAY), and membranes (PBI) were purchased without further processing. All chemicals were utilized without further purification.

Synthesis of the phosphonated polymers. The pentafluorophenyl-terminated p-terphenyl (PF-TP) was synthesized according to the established procedure described in the literature [1]. In a 10 mL round-bottomed flask, p-terphenyl (0.62 g, 2.7 mmol) was combined with PFBA (0.53 g, 2.7 mmol, 1 eq.). DCM (2.4 mL) and TFSA (0.6 mL) were subsequently added dropwise at room temperature under a nitrogen atmosphere. The resulting mixture was allowed to stir at room temperature until it became viscous. This viscous solution was then poured into methanol, completely washed by methanol and water, and dried under vacuum at 60 °C, affording a white fibrous polymer (PF-TP, 1.0 g, yield: 90.91%). The polymer (PF-PIM-SBI) with rigid and contorted chains is synthesized via the procedure similar to that of PF-TP except replacing p-terphenyl with the 6,6′-dimethoxy-3,3,3′,3′-tetramethyl-1,1′-spirobisindane (SBI) monomer.

The phosphonation of above two polymers was synthesized following previously established methods, affording PFPA-TP and PFPA-PIM-SBI [2, 3]. The synthesis involved the mixing of PF-TP (1.0 g, 2.45 mmol) and TSP (8.76 g, 29.41 mmol, 12 eq.) in a 50 mL round-bottomed flask, followed by heating the mixture to 170 °C and allowing it to react for 12 hours. Subsequently, the viscous solution was cooled to room temperature, diluted with THF (10 mL), and poured into hexane to precipitate a white product in trimethylsilyl ester form. The resulting polymer was filtered, washed with hexane (100 × 3 mL), and dried under vacuum at 40 °C overnight. The crude product was then treated with 1 M aqueous HCl solution and deionized water at 70 °C for 24 h, respectively. Finally, the white product was filtered and dried at 60 °C under vacuum for 24 h. PFPA-PIM-SBI was prepared by mixing PF-PIM-SBI (1.0 g, 1.95 mmol) with TSP (6.61 g, 23.34 mmol, 12 eq.), while the other procedures were the same.

Preparation of catalyst ink. The ink solution was prepared by firstly dispersing 0.1 g Pt/C (60 wt% Pt, HISPEC 9100, Johnson Matthey, for both cathode and anode) in 1 g deionized water and 4 g isopropanol, with 0.5 g binder solution (5 wt% ionomers in DMSO) added last. In this process, we also applied ultrasound to ensure rapid and uniform dispersion of the ionomer, and this dispersion was further subjected to ultrasonication for 30 minutes and stirring for 15 minutes, obtaining a well-dispersed catalyst ink.

Preparation of GDEs. The membrane electrode assemblies for fuel cell testing were prepared using the catalyst-coated substrate (CCS) method. The final GDEs had a catalyst loading of

0.50–0.07 mg_{Pt} cm^{-2} and a binder content of 20 wt% (based on the solid content in the catalyst ink). The as-prepared catalyst inks were inkjet printed onto the gas diffusion layer (GDL, Toray TGP-H-060). The catalyst loading in both the anode and cathode was controllable, and the final electrode area was 12.25 cm^2 (for 890e multi-range fuel cell test station, Scribner Associates, USA) or 4 cm^2 (for Lanmo tec, China). The end plates have serpentine flow fields.

NMR spectroscopy. ^1H, ^{19}F, and ^{31}P NMR spectra of the SBI, PF-TP, PF-PIM-SBI, PFPA-TP and PFPA-PIM-SBI were obtained using a Bruker Avance III HD 400 M spectrometer, with $CDCl_3$ or DMSO-d_6 as the solvent. For the PA-doped PBI membrane, the ^{31}P NMR spectra were acquired using a 600 MHz WB solid-state NMR spectrometer (Bruker Avance neo 600 wb).

ATR-FTIR (Attenuated total reflection Fourier transform infrared spectrometer) spectroscopy. ATR-FTIR spectra of samples were measured at a resolution of 2 cm^{-1} in the range of 4000 cm^{-1} to 600 cm^{-1}, with 64 scans for each spectrum (Thermo Nicolet FTIR spectrometer, USA).

Micropore characterization. Nitrogen sorption and desorption of polymers were obtained at 77.3 K using a JW-BK200C High-Speed Automated Surface Area and Pore Size Analyzer (JWBK Sci & Tech Co., China). Carbon dioxide (CO_2) sorption and desorption of polymer were carried out at 273.15 K (ASAP 2020, Micromeritic Instrument Corp., USA).

Dynamic vapor sorption (DVS). The water sorption behavior of samples was assessed using a dynamic vapor sorption (DVS) instrument (Aquadyne DVS-1 device) at 25 °C and varied relative humidity (RH) values. Before testing, the samples underwent overnight drying at 120 °C to eliminate moisture. The instrument automatically controlled the RH within a range of 0% to 90%, with a 2-hour hold at each stage to ensure water equilibrium.

Proton conductivity. The proton conductivity of the fully hydrated membrane samples was measured using a four-point probe AC electrochemical impedance spectroscopy on a Zahner Zennium E (Germany) electrochemical workstation in galvanostatic mode, at temperatures ranging from 30 to 80 °C. Conductivity measurement was conducted with an AC amplitude of 10 μA and a frequency range of 1 MHz to 10 Hz. Membrane conductivity (σ) was calculated from:

$$\sigma = \frac{L}{R \times W \times d}$$

where L is the distance between the two Pt electrodes (1 cm), W and d are the thickness and width of the membrane sample, and R is the recorded membrane resistance.

Electrochemical measurements and analysis. The Electrochemical Impedance Spectroscopy (EIS) resistance of the MEA was investigated using the Zahner Zennium E (Germany) electrochemical workstation. EIS was conducted in Potentiostatic Mode at a given voltage of 0.6 V with an AC signal amplitude of 5 mV. Impedance spectra were obtained by sweeping frequencies across the range of 0.01 Hz–10 kHz, with 10 points collected per decade. The experimental EIS spectra were analyzed using equivalent circuits and the Zview® software

from Scribner Associates. The applied equivalent circuit consists of a resistance (R_Ω) in series with one parallel capacitance/resistance circuit. The resistance (R_Ω) accounts for the ohmic losses, while the parallel circuit models the activation polarization, i.e. the charge transfer resistance.

The rotation disk electrode (RDE) characterization was conducted with the use of a CHI7052E electrochemical workstation facility, employing standard three-electrode systems. The working electrode consisted of an RDE with an active area of 0.196 cm^2 coated with catalyst ink, having a Pt loading of 0.1 mg cm^{-2}. The counter electrode was a Pt plate, and the reference electrode was an Ag/AgCl electrode. Polarization curves for the oxygen reduction reaction (ORR) were generated in an oxygen-saturated 0.1 M $HClO_4$ solution, with varied rotation speeds and a scan rate of 10 mV s^{-1}. These measurements were conducted at room temperature, and all potentials were normalized to the reversible hydrogen electrode (RHE) using the following equation:

$$E_{RHE}=E_0\ (Ag/AgCl) + 0.059pH + E\ (Ag/AgCl)$$

where $E_0(Ag/AgCl)$ is 0.197 V vs SHE. The kinetic current density (j_K) was calculated with Koutecky-Levich equation:

$$1/j=1/j_K+1/j_L$$

Where j is the apparent current density (mA cm^{-2}), and j_L is the limiting current density (mA cm^{-2}).

The cyclic voltammetry (CV) experiment involved the same electrochemical workstation and standard three-electrode systems as the RDE. H_2 and N_2 were provided to the anode and cathode at a flow rate of 0.2/0.2 L min^{-1} at room temperature. Before conducting the CV, the cathode was purged with dry N_2 for 10 minutes at a flow rate of 0.2 L min^{-1}. The CV was carried out at a scan rate of 20 mV s^{-1} and voltages ranging from 0.1 V to –0.9 V. The calculation of the electrochemical surface area (ECSA) was based on hydrogen desorption data, as per the following equation:

$$ECSA\ (m^2\ g_{Pt}^{-1}) = \frac{A(mA\ V)}{0.21(mC\ cm^{-2}) * V(mV\ s^{-1}) * M_{Pt}(g_{Pt})}$$

$$Pt\ utilization\ (\%) = \frac{ECSA\ (m^2\ g_{Pt}^{-1})}{85(m^2\ g_{Pt}^{-1})} \times 100$$

where A is the charge area, V is the scanning rate, M_{Pt} is the mass of loading Pt on the electrode, and 0.21 is the constant, 85 is the value of physical surface area of the 60% Pt/C catalyst.

Surface morphology. The surface morphology of the GDEs was obtained by using a scanning electron microscope (SEM, GeminiSEM 500) with an acceleration voltage of 20 kV. Transmission electron microscopy (TEM) images were captured using a JEM 2100F field emission TEM (JEOL Ltd., Akishima, Tokyo, Japan) at an accelerating voltage of 200 kV. The elements on the GDE surface were analyzed by the corresponding energy dispersive X-ray spectroscopy (EDS). Before testing, the catalyst ink, which was obtained by peeling off the

catalyst layer of the GDE and dispersed in an isopropanol/water mixture solvent, was diluted 10 times and dried onto an ultrathin copper grid.

Contact angle measurement. Contact angles of the membrane samples and GDE samples were recorded using static contact angle measurement on SL200B (Solon Tech Co., Ltd, China).

MEA fabrication. The PBI membranes were initially immersed in an 85 wt% phosphoric acid (PA) solution in a glass bath at 80 °C for 12 hours. Subsequently, the excess PA on the membrane surface was removed by tissue paper, and the doped membrane was subjected to a 12-hour drying process in a vacuum oven at 80 °C. PBI gas diffusion electrode (GDE) was processed by the same procedure as the membrane. Finally, the resulting PBI membrane was outfitted with GDEs on each side to create the membrane electrode assembly (MEA). The single fuel cell performances of PFPA-PIM-SBI based MEA and the control MEAs were investigated by using an 890e multi-range fuel cell test station (Scribner Associates, USA), at H_2/O_2 flow rate of 1.5/1.5 L min^{-1}, without backpressure and external humidification. The optimized single fuel cell performance of PFPA-PIM-SBI based MEA at the high temperature of up to 240 °C and varied Pt loading was evaluated by a test station (Lanmo tec, China), without backpressure and external humidification. The anode and cathode were fed with dry H_2 and O_2 at 0.5 L min^{-1}, respectively. The MEAs were first activated at a constant voltage of 0.6 V. Then, steady-state polarization curves and power density curves were recorded by setting the cell voltage from 1.0 V to 0.15 V in steps of 0.05 V, and holding the voltage for 30 s at each point. The long-term cycling stability of a single fuel cell was tested at the cell temperature of 160 °C, with H_2/O_2 flow rate of 0.2/0.2 L min^{-1}.

Pt-mass specific PPD (peak power density) (W mg_{Pt}^{-1}) was calculated from:

$$Pt-mass\ specific\ power\ density\ (W\ mg_{Pt}^{-1}) = \frac{Peak\ Pow\ density\ (W\ cm^{-2})}{Pt\ loading\ of\ the\ cathode\ (mg_{Pt}\ cm^{-2})}$$

The rated power was calculated to meet the Q/ΔT=1.45 kW $°C^{-1}$ target at the cell voltage (77.6/(22.1+T)). [4]

Simulation. Density-functional theory (DFT) calculations were conducted to study the adsorption energy of different ionomers on Pt (111) surface (the system consists of ionomer, Pt catalyst, and PA) by using the DMol module in the Materials Studio (MS) software (Biovia Inc) [5, 6].

Molecular dynamics (MD) simulations were carried out with a Forcite Plus of the MS software. The mixed systems of ionomers (50 repeating units), and oxygen molecules (150) were built by Amorphous Cell module. The mixed system model and Pt (111) surface model were combined through merging layers. The temperature was controlled to 433.15 K (operating temperature of the fuel cell) by a Nose-Hoover thermostat, and the pressure was controlled at 10 MPa. The force field was COMPASSII, and the time step was set as 1 ps. Finally, each system was simulated for 500 ps to reach equilibrium state.

Supplementary figures and tables

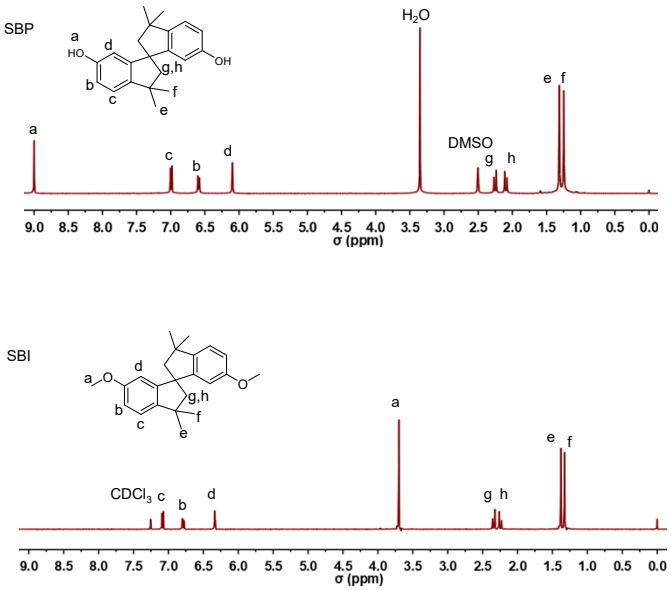

Supplementary Fig. S1. ^{1}H NMR spectra of SBP and SBI monomers.

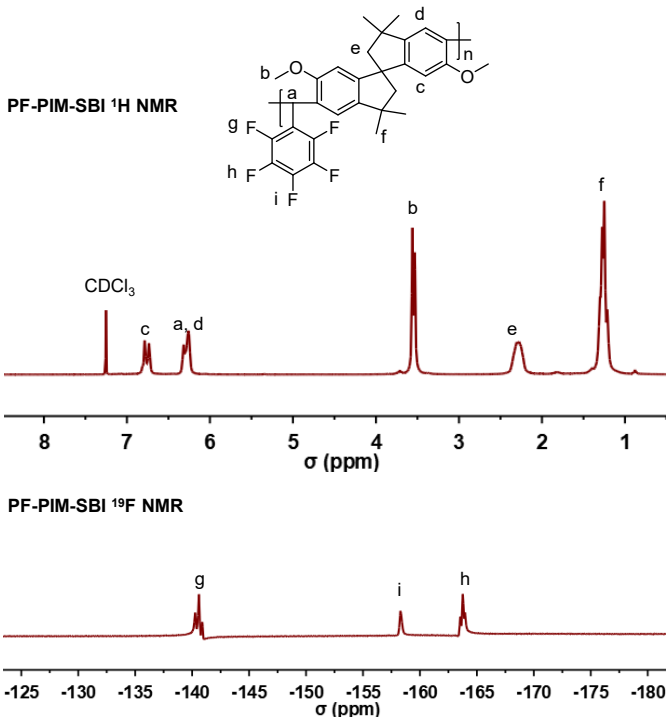

Supplementary Fig. S2. ^{1}H NMR and ^{19}F NMR spectra of PF-PIM-SBI ionomer.

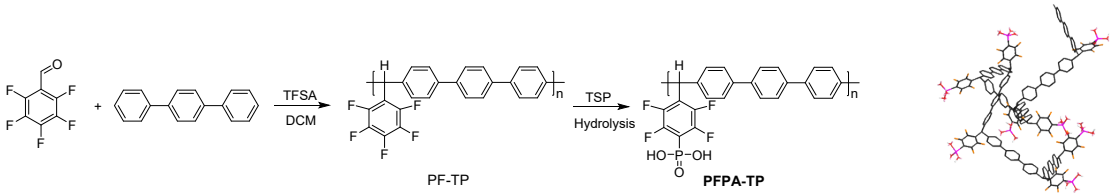

Supplementary Fig. S3. The synthesis and molecular configuration of PFPA-TP, which was synthesized via a superacid-catalyzed polyhydroxyalkylation, followed by phosphonation and subsequent hydrolysis. Model on the right shows the flexible molecular configuration of PFPA-TP.

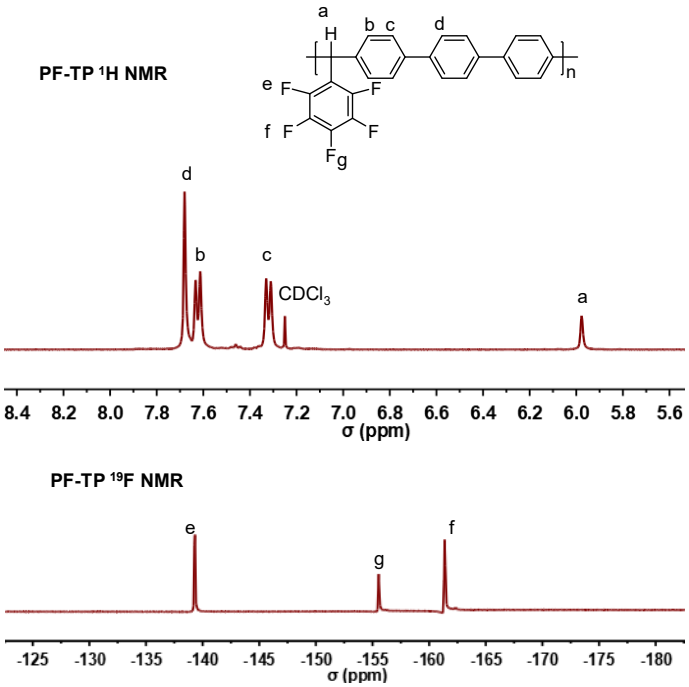

Supplementary Fig. S4. ^{1}H NMR and ^{19}F NMR spectra of PF-TP ionomer.

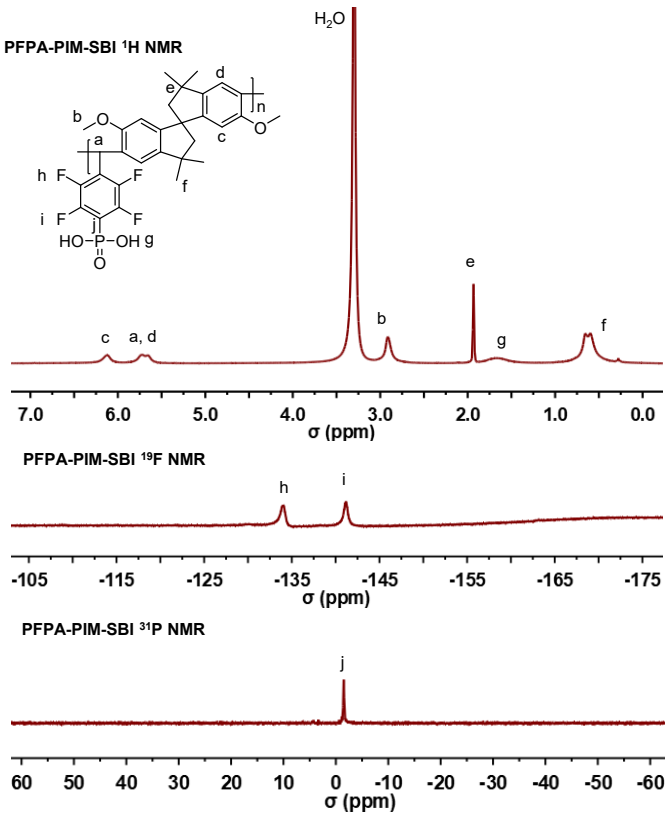

Supplementary Fig. S5. ^{1}H NMR, ^{19}F NMR and ^{31}P NMR spectra of PFPA-PIM-SBI ionomer.

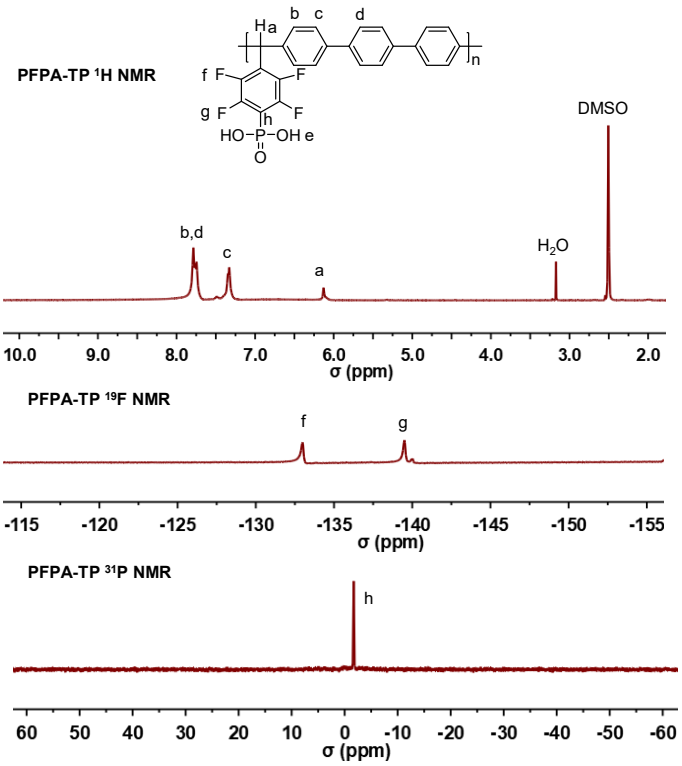

Supplementary Fig. S6. ^{1}H NMR, ^{19}F NMR and ^{31}P NMR spectra of PFPA-TP ionomer.

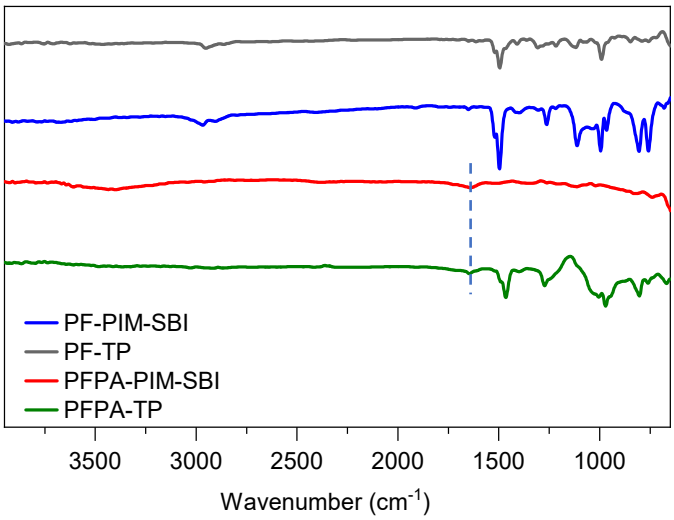

Supplementary Fig. S7. ATR-FTIR spectra of PF-PIM-SBI, PF-TP, PFPA-PIM-SBI and PFPA-TP ionomers. The characteristic peaks of (P) O-H···O=P (H bond) (1641 cm^{-1}) is presented with dotted line, indicating the phosphonation of PF-TP and PF-PIM-SBI.

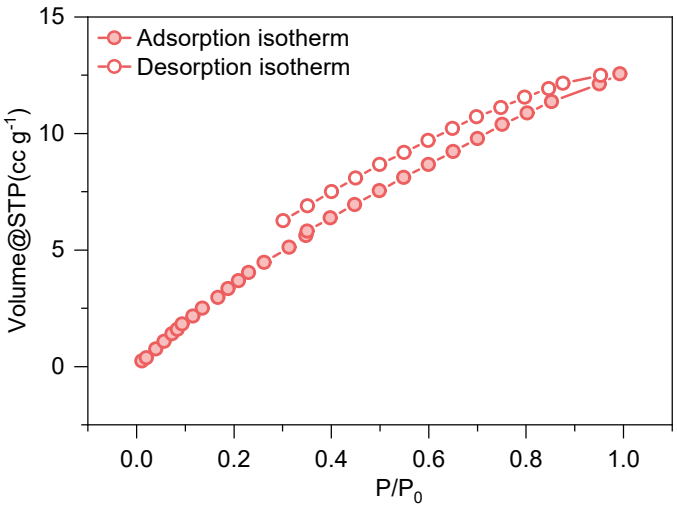

Supplementary Fig. S8. CO_2 adsorption-desorption isotherm of PFPA-PIM-SBI (273 K).

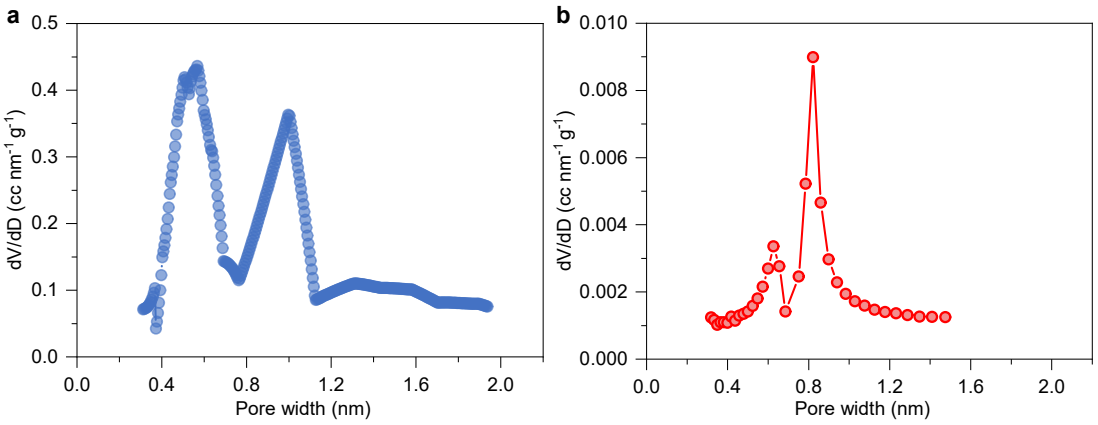

Supplementary Fig. S9. Pore size distributions of (a) PF-PIM-SBI polymer determined from N_2 adsorption-desorption experiment, and (b) PFPA-PIM-SBI polymer determined from CO_2 adsorption-desorption experiment.

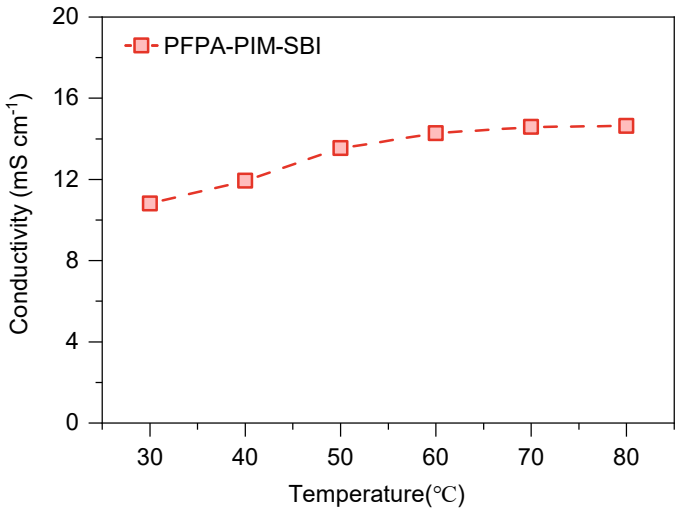

Supplementary Fig. S10. Proton conductivity of PFPA-PIM-SBI ionomer as a function of temperature.

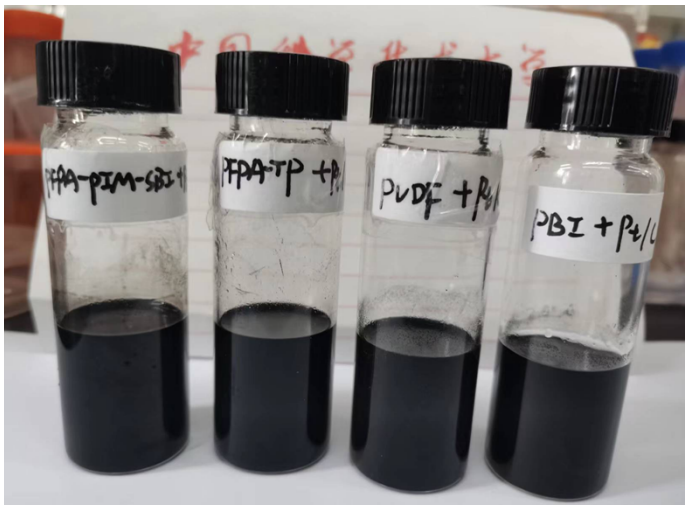

Supplementary Fig. S11. Photos of the catalyst ink dispersions prepared with different binders (PFPA-PIM-SBI, PFPA-TP, PVDF and PBI).

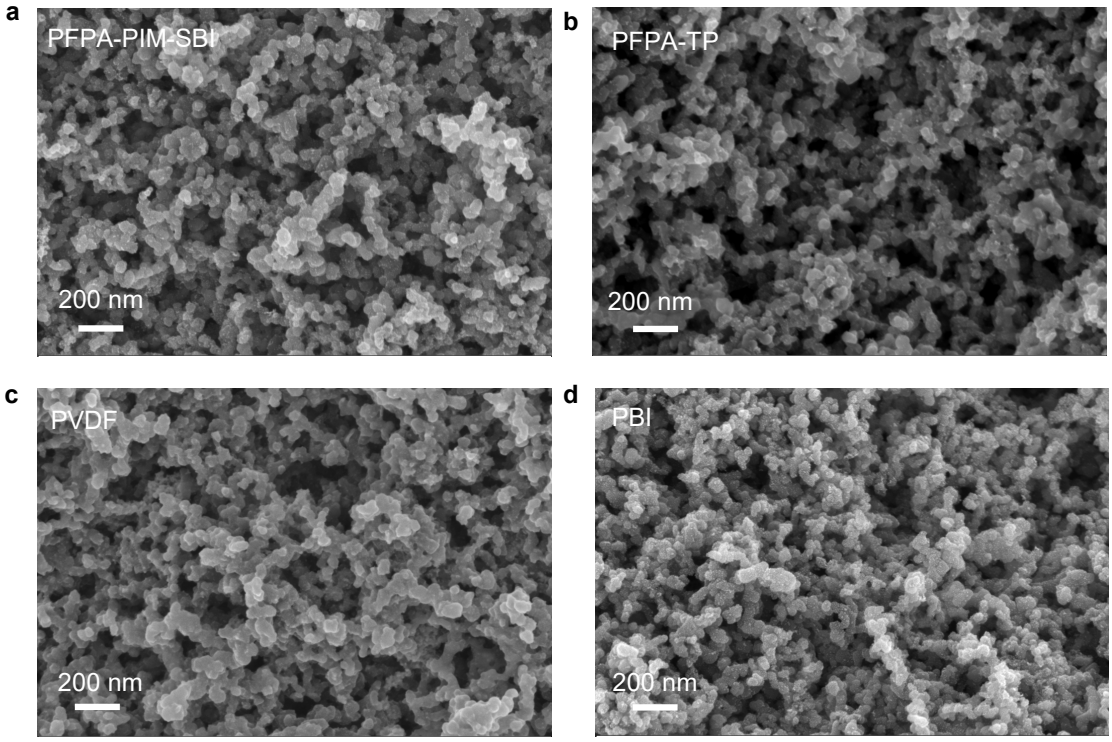

Supplementary Fig. S12. SEM images of the catalyst layer of gas diffusion electrodes (GDEs) prepared with (a) PFPA-PIM-SBI, (b) PFPA-TP, (c) PVDF and (d) PBI binders.

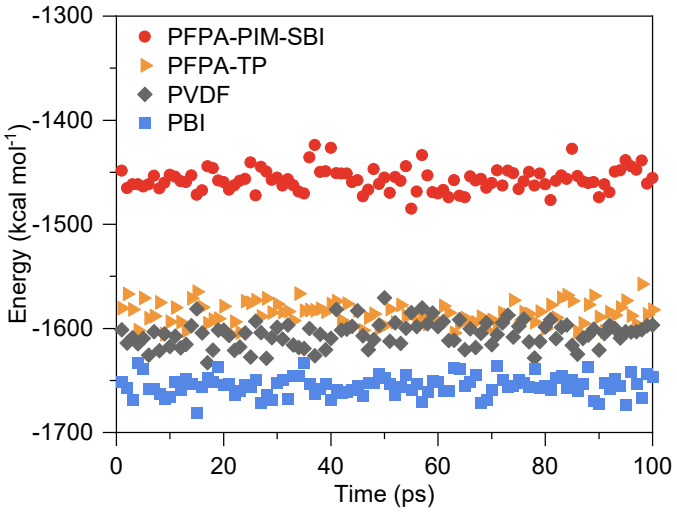

Supplementary Fig. S13. DFT optimized adsorption energies of PFPA-PIM-SBI, PFPA-TP, PVDF and PBI on the Pt catalyst surface (the system consists of ionomer, Pt catalyst, and PA).

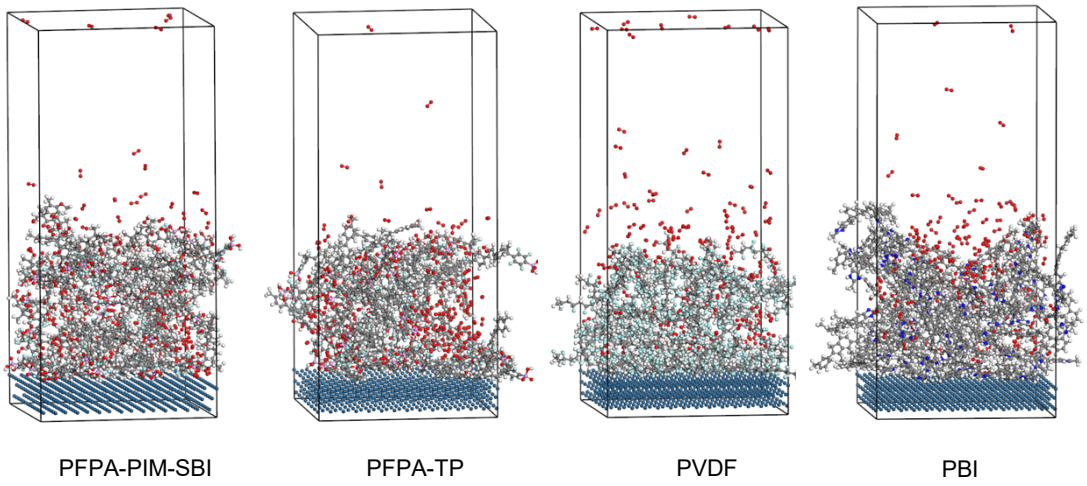

Supplementary Fig. S14. Three-dimensional O_2 equilibrium snapshots made by MD simulations for systems with varied ionomers (PFPA-PIM-SBI, PFPA-TP, PVDF and PBI). The white, red, brown, light aqua blue, deep navy blue, and blue in the molecular structures indicated H, O, C, F, N, and Pt atoms, respectively.

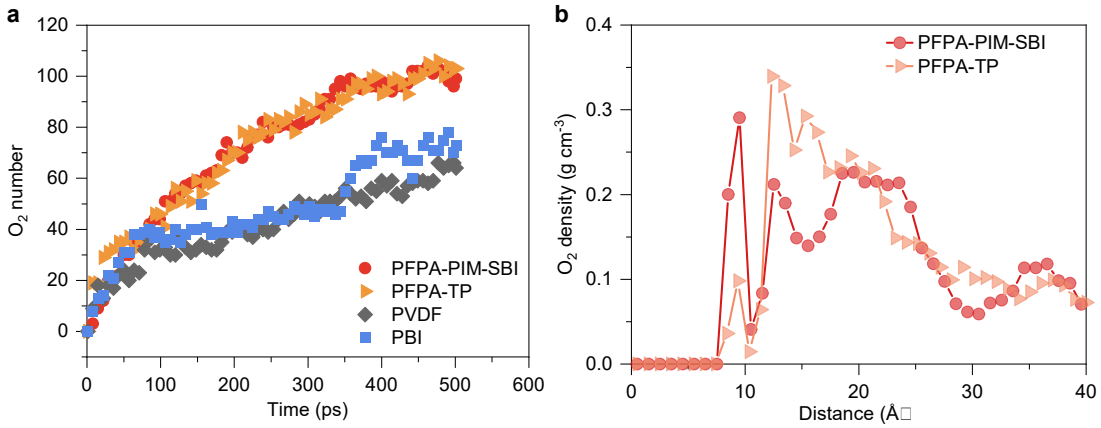

Supplementary Fig. S15. (a) The oxygen transport rate through the ionomer/Pt interface calculated by MD simulations for systems with varied ionomers (PFPA-PIM-SBI, PFPA-TP, PVDF and PBI). (b) The oxygen density distribution profiles of PFPA-PIM-SBI and PFPA-TP near the Pt surface (0-40 Å) (the counting zone of O_2 molecules in Supplementary Figure 15a).

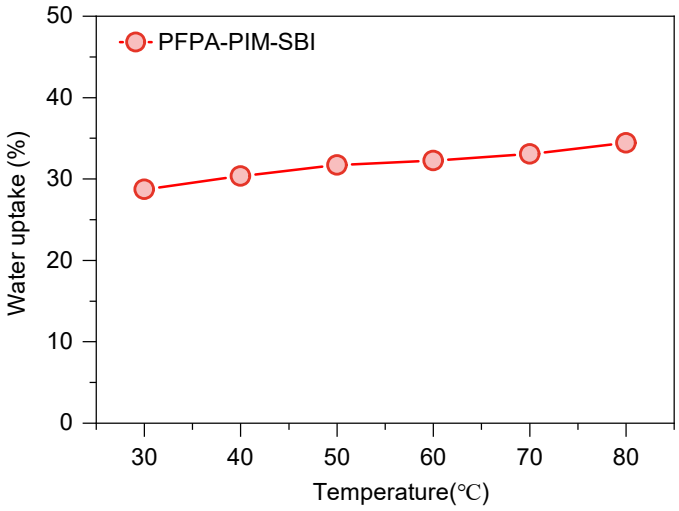

Supplementary Fig. S16. Water uptake of PFPA-PIM-SBI membrane as functions of temperature.

Supplementary Fig. S17. Linear sweep voltammograms (LSV) for the catalyst inks with varied ionomers: (a) PFPA-PIM-SBI, (b) PFPA-TP, (c) PVDF and (d) PBI. (e) LSV curves and (f) the Tafel slopes obtained from the TF-RDE test at 1600 rpm.

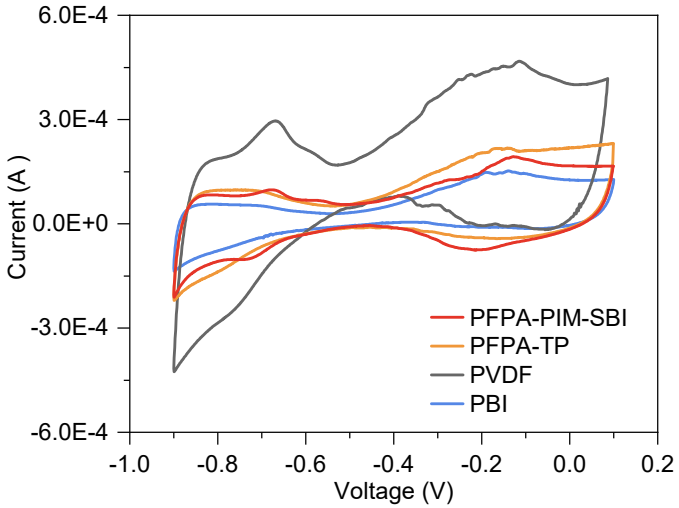

Supplementary Fig. S18. CV curves for the catalyst inks with varied ionomers: PFPA-PIM-SBI, PFPA-TP, PVDF and PBI.

Supplementary Fig. S19. Pt utilization and electrochemical surface area (ECSA) calculated from the cyclic voltammograms in **Supplementary Fig. S18**.

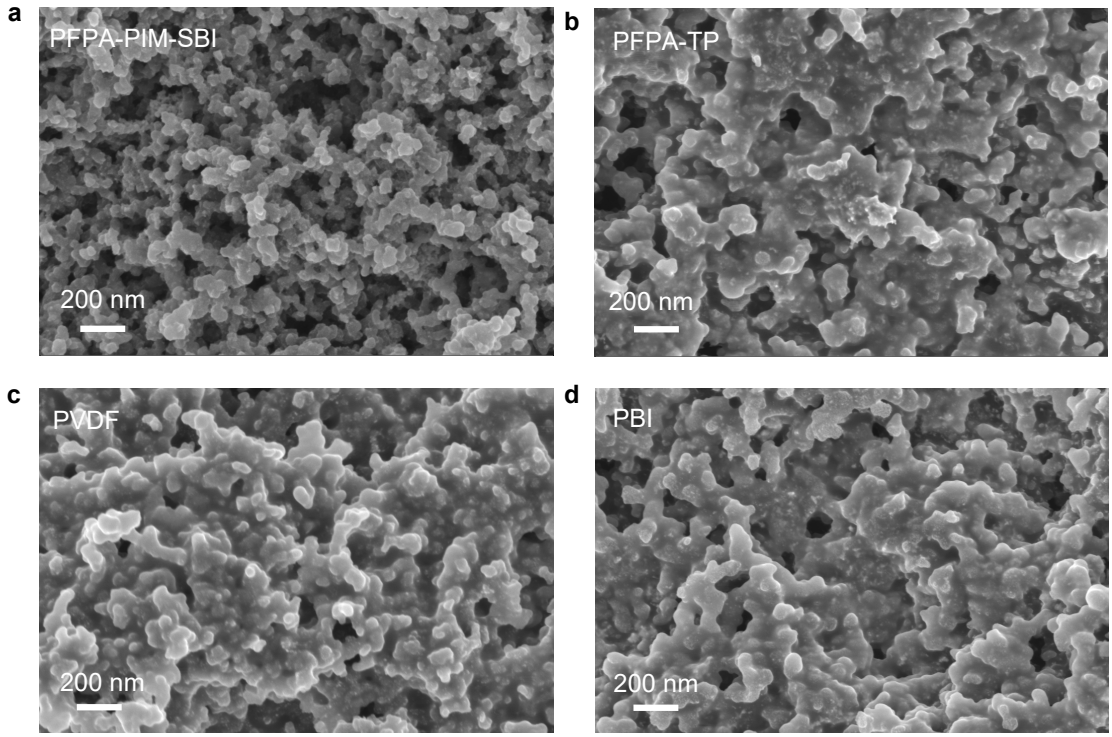

Supplementary Fig. S20. SEM images showing the surface morphologies for the GDEs with varied ionomers after MEA test: (a) PFPA-PIM-SBI, (b) PFPA-TP, (c) PVDF and (d) PBI.

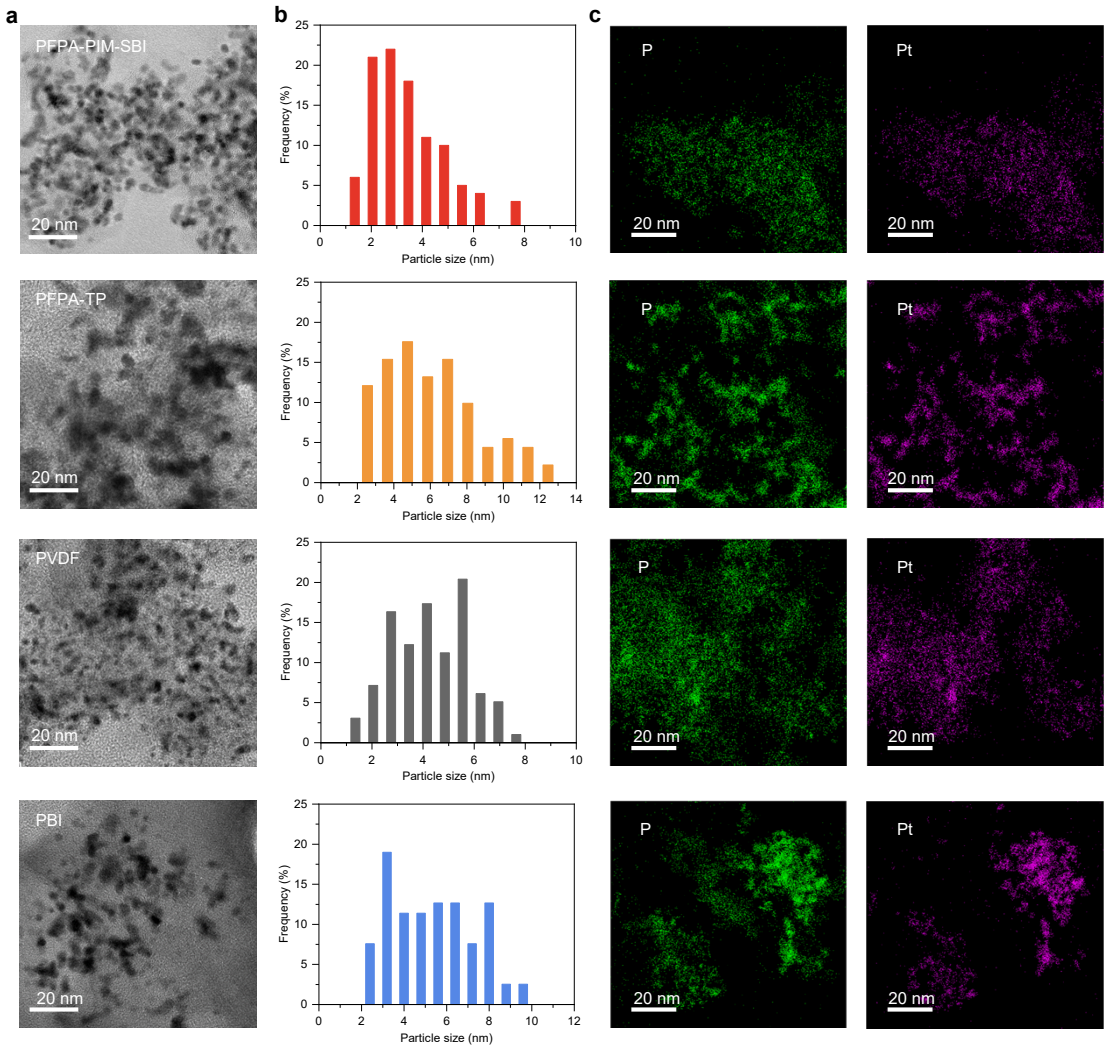

Supplementary Fig. S21. Micromorphology of the GDEs after MEA test. (a) TEM images, (b) the corresponding catalyst particle size distribution and (c) EDS patterns (phosphorous and platinum) for the GDEs coated with varied ionomers: PFPA-PIM-SBI, PFPA-TP, PVDF and PBI.

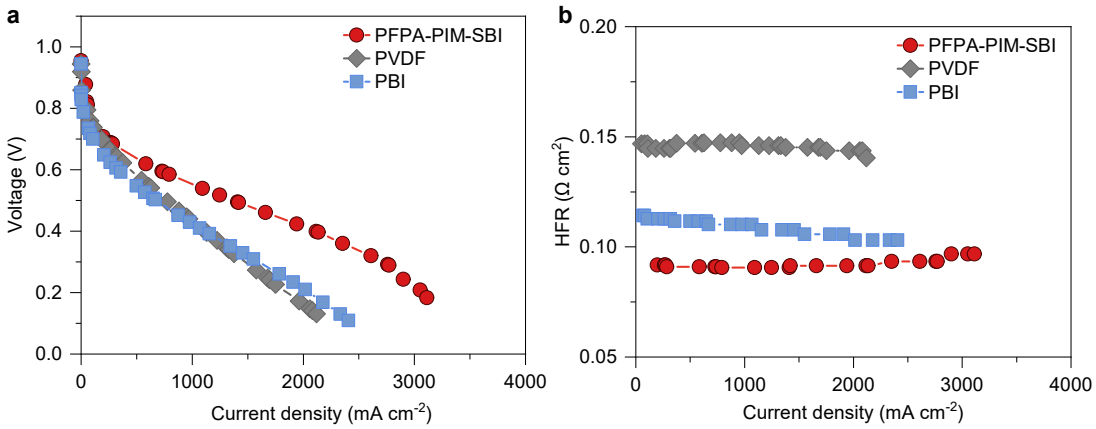

Supplementary Fig. S22. (a) Polarization and (b) High frequency resistance (HFR) curves measured for the MEAs assembled with PFPA-PIM-SBI, PVDF and PBI ionomeric binders at 160 °C. Test conditions: H_2/O_2 flow rate of 1.5/1.5 L min^{-1}, without backpressure and external humidification. For MEAs, the anode/cathode catalysts are Pt/C at a Pt loading of 0.50 mg cm^{-2}, and the membrane is PA-doped PBI membrane (thickness: 32 μm).

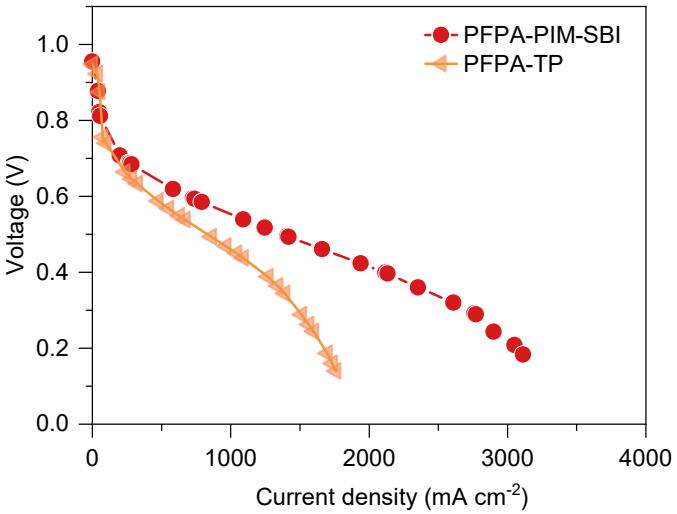

Supplementary Fig. S23. Polarization curves measured for the MEAs assembled with PFPA-PIM-SBI and PFPA-TP ionomeric binders at 160 °C. Test conditions: H_2/O_2 flow rate of 1.5/1.5 L min^{-1}, without backpressure and external humidification. For MEAs, the anode/cathode catalysts are Pt/C at a Pt loading of 0.50 mg cm^{-2}, and the membrane is PA-doped PBI membrane (thickness: 32 μm).

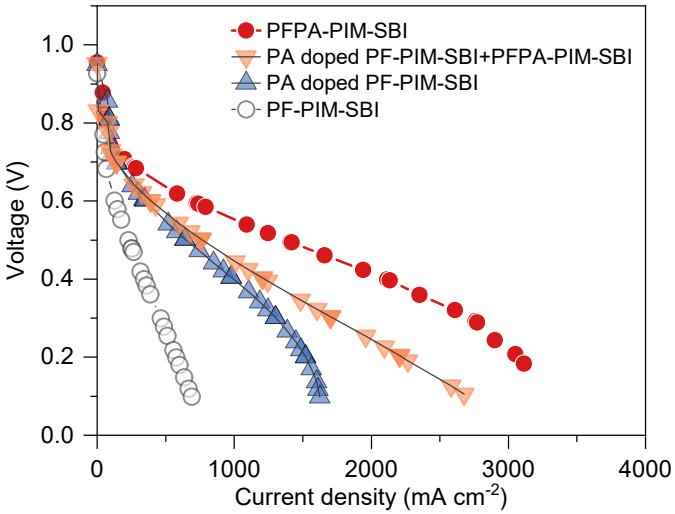

Supplementary Fig. S24. Polarization curves measured for the MEAs assembled with PFPA-PIM-SBI, PF-PIM-SBI, PA-doped PF-PIM-SBI and PA-doped a mixture of PF-PIM-SBI and PFPA-PIM-SBI (1:1) ionomeric binders at 160 °C. Test conditions: H_2/O_2 flow rate of 1.5/1.5 L min^{-1}, without backpressure and external humidification. For MEAs, the anode/cathode catalysts are Pt/C at a Pt loading of 0.50 mg cm^{-2}, and the membrane is PA-doped PBI membrane (thickness: 32 µm).

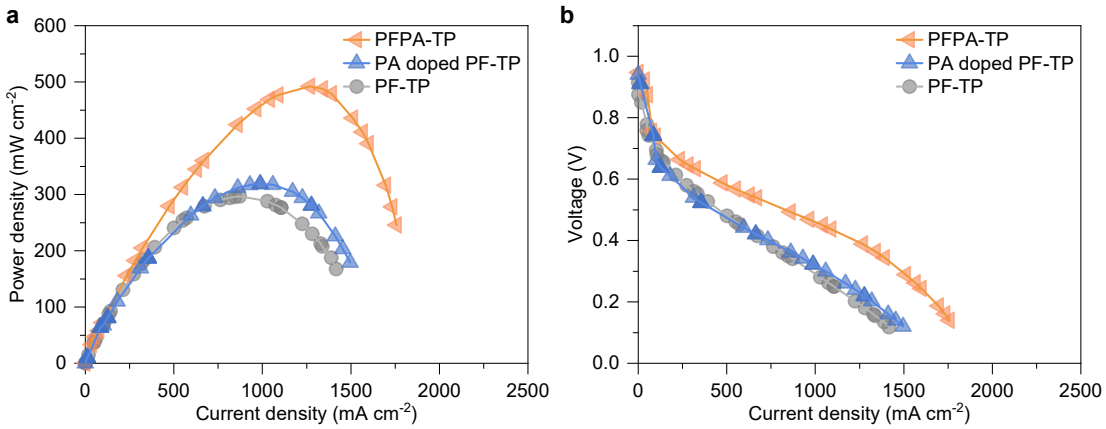

Supplementary Fig. S25. (a) Power density and (b) polarization curves measured at 160 °C for MEAs assembled with PFPA-TP, PA-doped PF-TP or PF-TP as MEA binders. Test conditions: H_2/O_2 flow rate of 1.5/1.5 L min^{-1}, without backpressure and external humidification. For MEAs, the anode/cathode catalysts are Pt/C at a Pt loading of 0.50 mg cm^{-2}, and the membrane is PA-doped PBI membrane (thickness: 32 μm).

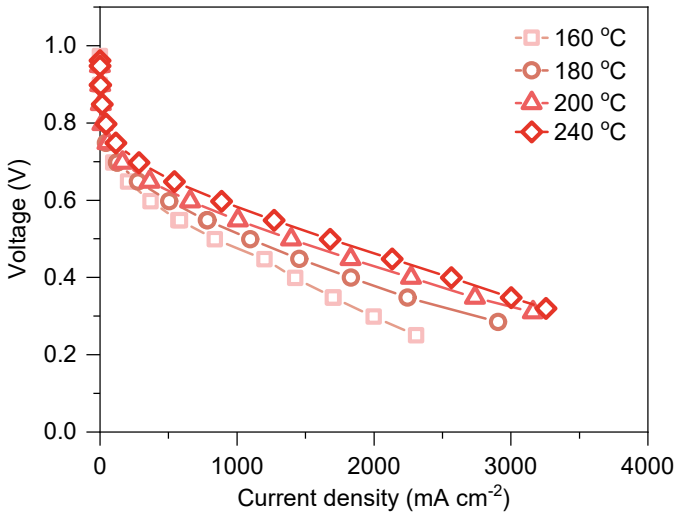

Supplementary Fig. S26. Polarization curves measured for the PFPA-PIM-SBI MEAs at elevated temperatures. Test conditions: H_2/O_2 flow rate of 0.5/0.5 L min^{-1}, without backpressure and external humidification. For MEAs, the anode/cathode catalysts are Pt/C at a Pt loading of 0.50 mg cm^{-2}, and the membrane is PA-doped PBI membrane (thickness: 32 µm).

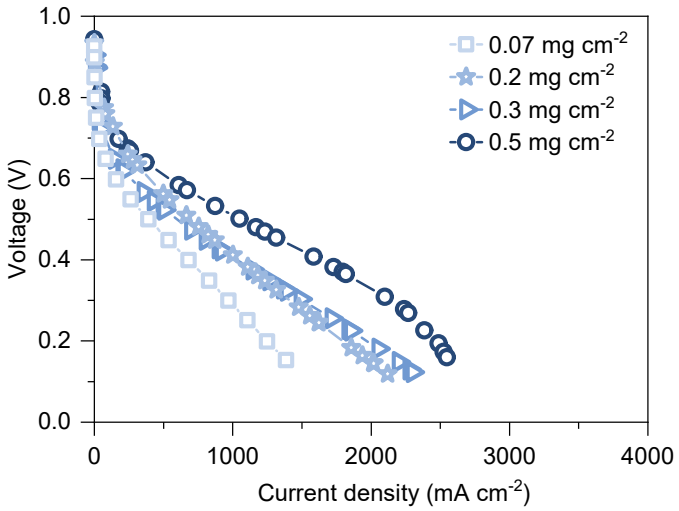

Supplementary Fig. S27. Polarization curves measured for the PFPA-PIM-SBI MEAs at varied Pt loadings (at 160 °C). Test conditions: H_2/O_2 flow rate of 0.5/0.5 L min^{-1}, without backpressure and external humidification. For MEAs, the anode/cathode catalysts are Pt/C, and the membrane is PA-doped PBI membrane (thickness: 32 µm).

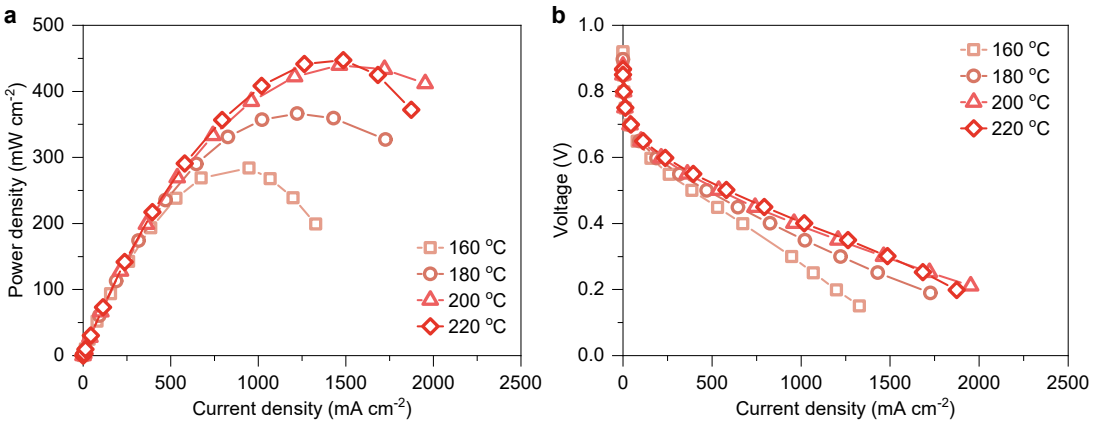

Supplementary Fig. S28. (a) Power density and (b) polarization curves measured for PFPA-PIM-SBI MEAs at elevated temperatures. Test conditions: H_2/O_2 flow rate of 0.2/0.2 L min^{-1}, without backpressure and external humidification. For MEAs, the anode/cathode catalysts are Pt/C at a Pt loading of 0.07 mg cm^{-2}, and the membrane is PA-doped PBI membrane (thickness: 32 µm).

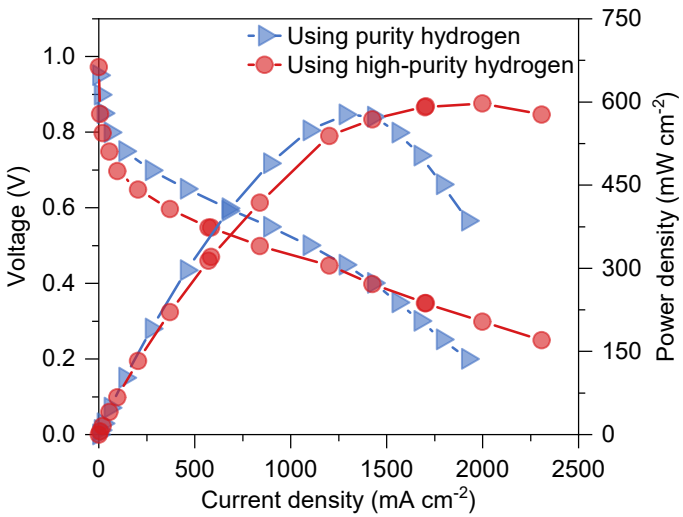

Supplementary Fig. S29. Power density and polarization curves measured for the PFPA-PIM-SBI based MEAs at 160 °C. Test conditions: H_2/O_2 (H_2 purity of 99.99%, containing 5 ppm CO or H_2 purity of 99.999%, containing 1 ppm CO, and O_2 purity of 99.999%) flow rate of 0.5/0.5 L min^{-1}, without backpressure or external humidification. For MEAs, the anode/cathode catalysts are Pt/C at a Pt loading of 0.50 mg cm^{-2}, and the membrane is PA-doped PBI membrane (thickness: 32 µm).

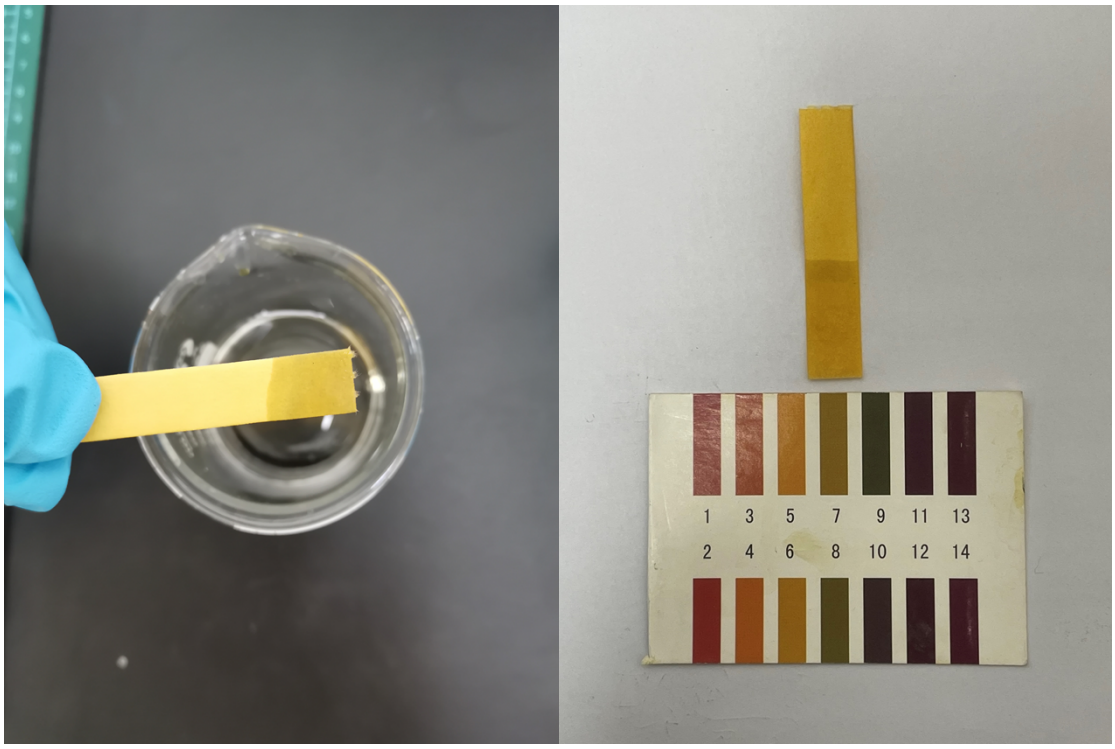

Supplementary Fig. S30. Photographs of pH indicators with the generated liquid exhausted from the end plates after the durability tests of 720 h. The pH indicators show no acid leaching.

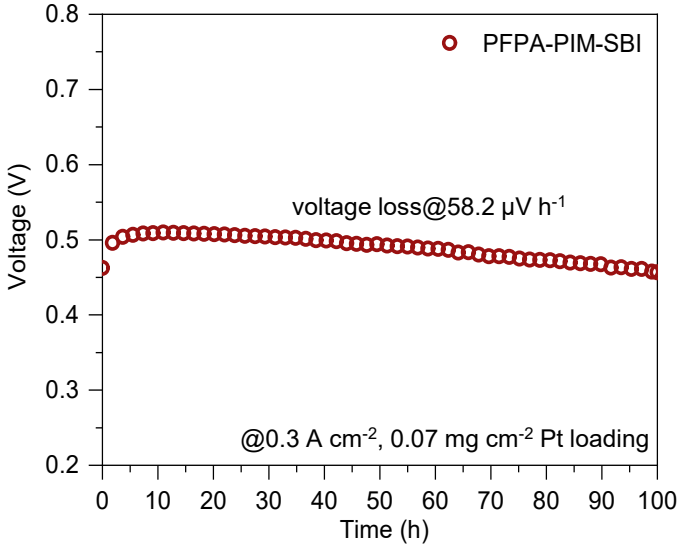

Supplementary Fig. S31. The cell voltage measured for PFPA-PIM-SBI MEA at a current density of 0.3 A cm^{-2} (at 160 °C). Test conditions: H_2/O_2 flow rate: 0.2/0.2 L min^{-1}, without backpressure and external humidification. For MEAs, the anode/cathode catalysts are Pt/C at a Pt loading of 0.07 mg cm^{-2}, and the membrane is PA-doped PBI membrane (thickness: 32 μm).

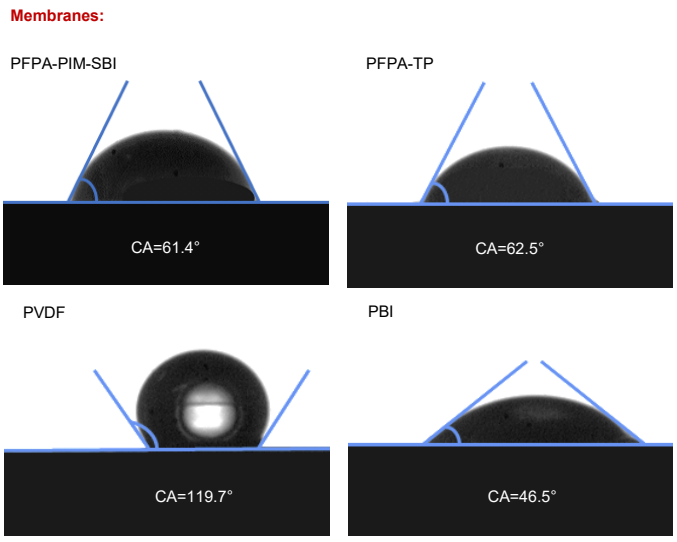

Supplementary Fig. S32. PA contact angles of membranes including PFPA-PIM-SBI, PFPA-TP, PVDF and PBI.

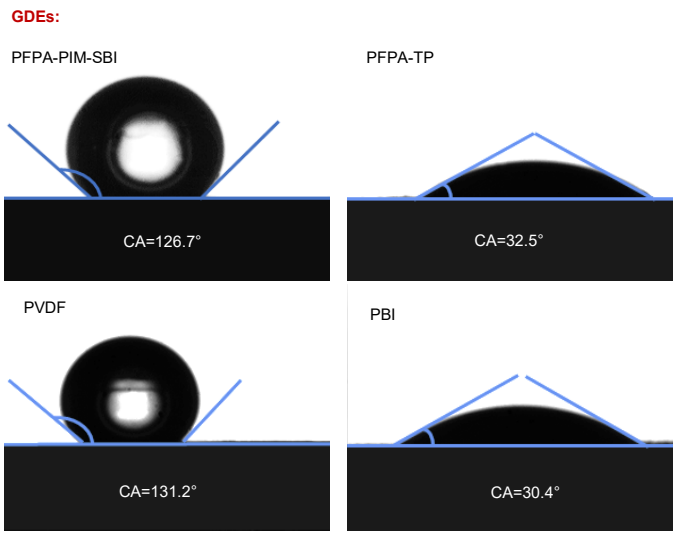

Supplementary Fig. S33. PA contact angles of GDEs including PFPA-PIM-SBI, PFPA-TP, PVDF and PBI.

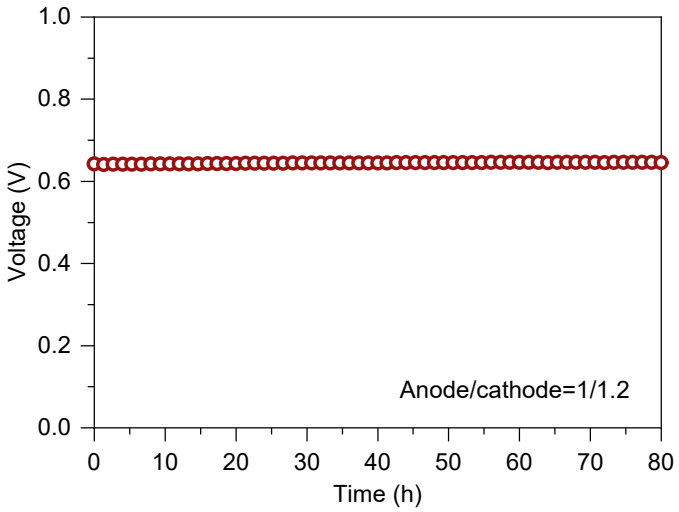

Supplementary Fig. S34. The cell voltage measured for PFPA-PIM-SBI MEA at a constant current density of 0.3 A cm^{-2} (at 160 °C). Test conditions: a fixed anode/cathode stoic of 1/1.2 (H_2/O_2 flow rate of 0.15/0.18 L min^{-1}), without backpressure or external humidification. For MEAs, the anode/cathode catalysts are Pt/C at a Pt loading of 0.5 mg cm^{-2}, and the membrane is PA-doped PBI membrane (thickness: 32 μm).

Supplementary Table S1. In-situ electrochemical analyses of the MEAs using varied ionomeric binders.

Binder	R_{Ω}* (Ω cm^2)	R_{ct} (Ω cm^2)	ECSA (m^2 g^{-1})	Pt utilization (%)
PBI	1.16	0.54	10.86	12.78
PVDF	1.14	0.69	10.77	12.67
PFPA-TP	1.09	0.43	22.02	25.90
PFPA-PIM-SBI	1.15	0.20	42.19	49.64

* R_{Ω} of the MEA is primarily caused by the ionic resistance of the membrane. Since all MEAs in this study utilize the same commercial PBI membranes, the R_{Ω} values for the four MEAs are similar, measuring around 1.1 Ω cm^2.

Supplementary Table S2. Comparison of the H_2/O_2 performance of representative HT-PEMFCs.

Membrane	Binder	Pt loading (mg cm^{-2}) Anode/Cathode	Rated (0.43 V)		0.7 V		Peak		Operating temperature (°C)	Reference
			Current density (mA cm^{-2})	Power density (mW cm^{-2})	Current density (mA cm^{-2})	Power density (mW cm^{-2})	Current density (mA cm^{-2})	Power density (mW cm^{-2})		
mPBI	PFPA-PIM-SBI	0.5/0.5	1934	824	288	202	2353	846	160	This work
mPBI	PVDF	0.5/0.5	1018	434	181	127	1311	453	160	This work
mPBI	PBI	0.5/0.5	958	408	112	78	1552	481	160	This work
mPBI	PTFE	0.5/0.5	631	269	52	36	1226	396	160	[7]
Trip-TB	PTFE	0.5/0.5	961	409	130	91	1372	489	160	[7]
DMBP-TB	PTFE	0.5/0.5	1633	696	170	119	2231	815	160	[7]
QAPOH	QASOH	0.5/0.6	1050	447	137	96	993	441	160 (206.8 kpa)	[8]
mPBI	PWN70	0.5/0.6	1246	531	295	207	1552	527	160 (147.1 kpa)	[9]
mPBI	PTFE	1.0/0.75	1721	733	344	241	1849	730	160 (147.1 kpa)	[9]
mPBI	PIM-Tz	0.5/0.5	1738	740	231	162	2463	828	160	[10]

Supplementary Table S3. Summary and comparison of the H_2/O_2 performance of representative PA-PBI-based HT-PEMFC at 160 °C.

Membrane	Binder	Pt loading (mg_{Pt} cm^{-2}) Anode/Cathode	PPD (mW cm^{-2})	Pt mass-specific PPD (W mg_{Pt}^{-1})	Reference
*m*PBI	PFPA-PIM-SBI	0.5/0.5	663	1.33	This work
*m*PBI	PFPA-PIM-SBI	0.3/0.3	452	1.51	This work
*m*PBI	PFPA-PIM-SBI	0.2/0.2	429	2.15	This work
*m*PBI	PFPA-PIM-SBI	0.07/0.07	290	4.15	This work
*m*PBI	PFPA-TP	0.5/0.5	419	0.84	This work
*m*PBI	PVDF	0.5/0.5	464	0.93	This work
*m*PBI	PBI	0.5/0.5	344	0.69	This work
Cross-linked PBI-30/PA	PBI	0.6/0.6	533	0.89	[11]
Cross-linked PBI-20/PA	PBI	0.6/0.6	467	0.79	[11]
Grafted-20 PBI/PA	PBI	0.6/0.6	443	0.74	[12]
*m*PBI	PBI	0.58/0.58	383	0.66	[13]
OHPyPBI	PBI	0.58/0.58	523	0.90	[13]
PBI-1	PBI	0.5/0.5	305	0.61	[14]
PBI-2	PBI	0.5/0.5	244	0.49	[14]
PBI-EP-151	PBI	0.5/0.5	358	0.72	[14]
PBI-EP-101	PBI	0.5/0.5	342	0.68	[14]
Be3Br-7.5%-PBI	PBI	0.58/0.58	~340	0.59	[15]
C-PBI-20 -SiO_2-2	PBI	0.6/0.6	497	0.83	[16]
P1	mPBI	0.6/0.8	907	1.51	[17]
P2	mPBI	0.6/0.8	748	1.25	[17]

PIM-1 reinforced PBI alloy membranes	OPBI	0.6/0.6	438	0.73	[18]
PDA-PBI	PDA-PBI	0.6/0.6	460	0.77	[19]
*m*PBI	F6PBI	0.5/0.5	705	1.41	[20]
*m*PBI	F4PBI	0.5/0.5	648	1.30	[20]
*m*PBI	Trip-PBI	0.5/0.5	700	1.40	[21]
PBI-SPOSS	Ph-PBI	0.6/0.6	300	0.50	[22]
OPBI	PBPBI-3CN	1.0/1.0	804	0.80	[23]
40%UIO-66@PBI	PBPBI-3CN	1.0/1.0	716	0.72	[23]
OPBI@1sMXene	PTFE	1.0/1.0	592	0.59	[24]
OPBI@3sMXene	PTFE	1.0/1.0	660	0.66	[24]
OPBI-CL-Pillar-7%	PTFE	0.6/0.6	923	1.54	[23]
Br*p*PBI-*b*-F6-PBI	PTFE	1.0/1.0	713	0.71	[25]
BrF6-PBI-*b*-*p*PBI	PTFE	1.0/1.0	~550	0.55	[25]
*m*PBI	P-PPSU-2.75	0.5/0.5	242	0.48	[26]
*m*PBI	ESFE	0.5/1.0	640	1.28	[27]
*m*PBI	PIM-Tz	0.5/0.5	828	1.70	[10]
*m*PBI	PIM-Tz	0.35/0.35	832	2.40	[10]
*m*PBI	PIM-Tz	0.15/0.15	570	3.80	[10]

Supplementary Table S4. Summary and comparison of the H_2/O_2 performance of representative hydrocarbon-based HT-PEMFC at 160 °C.

Membrane	Binder	Pt loading ($mg_{Pt}\ cm^{-2}$) Anode/Cathode	PPD ($mW\ cm^{-2}$)	Pt mass-specific PPD ($W\ mg_{Pt}^{-1}$)	Reference
DMBP-TB/PEKC	PBI	0.7/0.7	~485	0.69	[28]
P-g-V-x	PTFE	0.45/0.45	559	1.24	[29]
PSf-TEA-110	PTFE	0.65/0.65	~425	0.65	[30]
PSf-TMA-110	PTFE	0.65/0.65	~410	0.63	[30]
PES–PVP–BN	PTFE	0.65/0.65	359	0.55	[31]
DMBP-TB	PTFE	0.5/0.5	815	1.63	[7]
PAP-BP-80-iBu	PTFE	0.5/1.5	1228	2.46	[32]
PAP-BP-80-iBu	PTFE	0.5/1.5	1651 (80KPa)	3.30	[32]
P/CN-0.5(CN-doped PES/PVP)	PTFE	0.4/0.4	512	1.28	[33]
PES/PVP	PTFE	0.35/0.35	637	1.82	[34]
TABPP	PTFE	1.0/1.0	760	0.76	[35]
PVDF-PVP-80	PVP	0.5/0.5	~430	0.86	[36]
QAPOH	QASOH	0.6/0.6	~450	0.75	[8]
QAPOH	PWN	0.5/0.6	1130 (147.1KPa)	1.88	[9]
QAPOH	PWN/Nafion	0.5/0.7	1673 (148KPa)	2.38	[37]

Supplementary Table S5. Summary and comparison of the durability performance of representative HT-PEMFC. (reactants: H_2-O_2)

Membrane	Binder	Pt loading (mg_{Pt} cm^{-2}) Anode/Cathode	Durability/Degradation rate	Reference
*m*PBI	PFPA-PIM-SBI	0.5/0.5	720 h; stable (0.3 A cm^{-2}) 3 start-up/shutdowns	This work
*m*PBI	PFPA-PIM-SBI	0.07/0.07	100 h; 58.2 μV h^{-1} (0.3 A cm^{-2})	This work
*m*PBI	PIM-Tz	0.5/0.5	800 h; stable (0.3 A cm^{-2})	10
*m*PBI	PIM-Tz	0.35/0.35	600 h; stable (0.3 A cm^{-2}) (H_2-air)	10
p-PBI sol-gel membranes	E-Tek GDE	＞1.0/1.0	＞1000 h; 43 μV h^{-1} (0.4 A cm^{-2})	38
Celtec®-P 1000	BASF GDE	0.75-1.0/0.75-1.0	＞6000 h; 5-6 μV h^{-1} (0.3 A cm^{-2})	39
Poly (aryl sulfone benzimidazole)	HCOOH, PA and *m*PBI	0.7/0.7	＞2400 h; 2.4-6.4 μV h^{-1} (0.3 A cm^{-2})	40
PBI	HCOOH, PA and *m*PBI	0.6/0.6	＞1500 h; 1.5 μV h^{-1} (0.3 A cm^{-2})	41
Cross-liked-6F PBI	HCOOH, PA and *m*PBI	0.6/0.6	2600 h; 63 μV h^{-1} (0.3 A cm^{-2})	42
Thermoset *m*PBI	*m*PBI	0.58/0.29	＞2000 h; 5-6 μV h^{-1} (0.2 A cm^{-2}); 43μV h^{-1} (0.6 A cm^{-2})	43
So-gel PBI (BASF)	BASF GDE	0.7/1.0	＞6000 h; 4.9-6.3 μV h^{-1} (0.2 A cm^{-2})	44
PBI & PBI-O-PhT + Zr $(Acac)_4$ composite	BASF GDE	1.0/1.0	＞2000 h; stable (0.4 A cm^{-2})	45
OPBI	Nafion	1.5/1.5	780 h; ~ 25 μV h^{-1} (0.2 A cm^{-2})	46

PyPBI	BASF GDE	1.0/1.0	2300 h; 5.2 μV h^{-1} (0.2 A cm^{-2})	47
PBI	PVDF	0.8/0.8	17860 h; < 4 μV h^{-1} (0.2 A cm^{-2})	48
Cross-liked AB-PBI	PVDF	0.8/0.8	17500 h; < 4 μV h^{-1} (0.2 A cm^{-2})	49
PBI MEA (BASF)	BASF GDE	＞1.0/1.0	4000 h; 19 μV h^{-1} (0.2 A cm^{-2}); 157 start-up/shutdowns; 480 μV/cycle	50
Sulfonated PBI	BASF GDE	1.0/1.0	~ 3000 h; 30 μV h^{-1} (0.2 A cm^{-2})	51
OPBI-CL-Pillar-7%	PTFE	0.6/0.6	200 h; 39.5 μV h^{-1} (0.2 A cm^{-2})	52
OPBI	PBI	1.0/1.0	200 h; 0.182 mV h^{-1} (0.2 A cm^{-2})	23
OPBI	PBPBI-3CN	1.0/1.0	200 h; 0.069 mV h^{-1} (0.2 A cm^{-2})	23
PSF-QA	PTFE	0.55/0.55	< 30 h (0.2 A cm^{-2})	30
*/w*PBI	Phosphonated PPSU	0.5/0.5	200 h; stable (0.2 A cm^{-2})	26
PAP-BP-80-iBu	PTFE	0.5/1.5	1000 h, stable (0.2 A cm^{-2}, 120 ℃)	32
QAPOH	PWN70	0.5/0.6	>550 h, 0.35 μV h^{-1} (0.6 A cm^{-2}, 160 °C, H_2-air, 147.1 kPa)	9
QAPOH	Nafion-PWN-1.8	0.5/0.6	200 h, stable (0.2 A cm^{-2}, 80 °C, H_2/air=72:30, 148 kPa); 2500 h, stable (0.6 A cm^{-2}, 160 °C, H_2/air=24:10, 148 kPa)	37
Nafion N212	Pt/C@SDT-	0.05/0.07	65 h, stable	53

	Nafion		(OCV, 90 °C）	
Nafion HP	Cyclohexanol-Nafion	0.08/0.12	15 h stable (H_2-air at 0.6 V, 80 °C)	[54]
SSC PFSA	PTFE	0.4/0.4	120 h, retain 80% (OCV, 90 °C and 30% RH)	[55]

Reference:

1. V. M. Velasco, M. G. Zolotukhin, M. T. Guzmán-Gutiérrez, S. L. Morales, S. Fomine, M. P. Carreón-Castro, M. Salmón and U. Scherf, *Macromolecules*, 2008, **41**, 8504-8512.
2. X. Sun, J. Guan, X. Wang, X. Li, J. Zheng, S. Li and S. Zhang, *ACS Cent. Sci.*, 2023, **9**, 733-741.
3. N. R. Kang, T. H. Pham, H. Nederstedt and P. Jannasch, *J. Membr. Sci.*, 2021, **623**, 119074.
4. United States Driving Research and Innovation for Vehicle efficiency and Energy sustainability Partnership, *Fuel Cell Technical Team Roadmap*, U.S. Department of Energy, 2017.
5. W. Yu, J. Zhang, D.-M. Huang, X. Liang, K. Zhang, Y. Xu, H. Zhang, B. Ye, X. Ge, T. Xu and L. Wu, *ACS Energy Lett.*, 2023, **8**, 790-799.
6. S. Maurya, S. Noh, I. Matanovic, E. J. Park, C. Narvaez Villarrubia, U. Martinez, J. Han, C. Bae and Y. S. Kim, *Energy Environ. Sci.*, 2018, **11**, 3283-3291.
7. H. Tang, K. Geng, L. Wu, J. Liu, Z. Chen, W. You, F. Yan, M. D. Guiver and N. Li, *Nat. Energy*, 2022, **7**, 153-162.
8. K.-S. Lee, J. S. Spendelow, Y.-K. Choe, C. Fujimoto and Y. S. Kim, *Nat. Energy*, 2016, **1**, 16120.
9. V. Atanasov, A. S. Lee, E. J. Park, S. Maurya, E. D. Baca, C. Fujimoto, M. Hibbs, I. Matanovic, J. Kerres and Y. S. Kim, *Nat. Mater.*, 2021, **20**, 370-377.
10. H. Tang, K. Geng, D. Aili, Q. Ju, J. Pan, G. Chao, X. Yin, X. Guo, Q. Li and N. Li, *Nat. Commun.*, 2022, **13**, 7577.
11. X. Li, H. Ma, P. Wang, Z. Liu, J. Peng, W. Hu, Z. Jiang, B. Liu and M. D. Guiver, *Chem. Mater.*, 2020, **32**, 1182-1191.
12. X. Li, P. Wang, Z. Liu, J. Peng, C. Shi, W. Hu, Z. Jiang and B. Liu, *J. Power Sources*, 2018, **393**, 99-107.
13. J. Yang, Y. Xu, L. Zhou, Q. Che, R. He and Q. Li, *J. Membr. Sci.*, 2013, **446**, 318-325.
14. H.-L. Lin, Y.-C. Chou, T. L. Yu and S.-W. Lai, *Int. J. Hydrog. Energy*, 2012, **37**, 383-392.
15. J. Yang, H. Jiang, L. Gao, J. Wang, Y. Xu and R. He, *Int. J. Hydrog. Energy*, 2018, **43**, 3299-3307.
16. X. Li, H. Ma, P. Wang, Z. Liu, J. Peng, W. Hu, Z. Jiang and B. Liu, *ACS Appl. Mater. Interfaces*, 2019, **11**, 30735-30746.
17. P.-Y. Chen, T.-H. Chiu, F.-J. Lin and J.-C. Chen, *J. Membr. Sci.*, 2022, **654**, 120569.
18. P. Wang, X. Li, Z. Liu, J. Peng, C. Shi, T. Li, J. Yang, C. Shan, W. Hu and B. Liu, *J. Membr. Sci.*, 2022, **659**, 120790.
19. J. Fang, X. Lin, D. Cai, N. He and J. Zhao, *J. Membr. Sci.*, 2016, **502**, 29-36.
20. G. Chao, H. Tang, Q. Ju, N. Li and K. Geng, *J. Power Sources*, 2023, **556**, 232473.
21. Q. Ju, H. Tang, H. Dong, K. Geng, H. Qian, X. Ma and N. Li, *J. Membr. Sci.*, 2023, **683**, 121788.
22. J. Yang, X. Li, C. Shi, B. Liu, K. Cao, C. Shan, W. Hu and B. Liu, *J. Membr. Sci.*, 2021, **620**, 118855.

23. A. Gao, W. Wang, P. Wang, H. Wu, C. Gong, A. Wu, G. Wei and L. Wang, *Adv. Funct. Mater.*, 2023, **33**, 2305948.
24. X. Yan, Y. Liu, G. Wei, M. Shekh, C. Zhu and G. Zhu, *Mater. Today Chem.*, 2023, **34**, 101757.
25. L. Wang, Y. Wu, M. Fang, J. Chen, X. Liu, B. Yin and L. Wang, *J. Membr. Sci.*, 2020, **602**, 117981.
26. H. Tang, K. Geng, Y. Hu and N. Li, *J. Membr. Sci.*, 2020, **605**, 118107.
27. Z. Zhang, Z. Xia, J. Huang, F. Jing, X. Zhang, H. Li, S. Wang and G. Sun, *Sci. Adv.*, 2023, **9**, eade1194.
28. T. Wang, Y. Jin, T. Mu, T. Wang and J. Yang, *J. Membr. Sci.*, 2022, **654**, 120539.
29. H. Bai, H. Wang, J. Zhang, J. Zhang, S. Lu and Y. Xiang, *J. Membr. Sci.*, 2019, **592**, 117395.
30. H. Tang, K. Geng, J. Hao, X. Zhang, Z. Shao and N. Li, *J. Power Sources*, 2020, **475**, 228521.
31. B. Lv, H. Yin, Z. Huang, K. Geng, X. Qin, W. Song and Z. Shao, *J. Membr. Sci.*, 2022, **653**, 120512.
32. J. Li, C. Yang, X. Zhang, Z. Xia, S. Wang, S. Yu and G. Sun, *J. Mater. Chem. A*, 2023, **11**, 18409-18418.
33. H. Bai, H. Wang, J. Zhang, C. Wu, J. Zhang, Y. Xiang and S. Lu, *J. Membr. Sci.*, 2018, **558**, 26-33.
34. J. Zhang, H. Bai, W. Yan, J. Zhang, H. Wang, Y. Xiang and S. Lu, *J. Electrochem. Soc.*, 2020, **167**, 114501.
35. X. Hu, Y. Ao, Y. Gao, B. Liu and C. Zhao, *J. Membr. Sci.*, 2023, **687**, 122102.
36. Z. Guo, X. Xu, Y. Xiang, S. Lu and S. P. Jiang, *J. Mater. Chem. A*, 2015, **3**, 148-155.
37. K. H. Lim, A. S. Lee, V. Atanasov, J. Kerres, E. J. Park, S. Adhikari, S. Maurya, L. D. Manriquez, J. Jung, C. Fujimoto, I. Matanovic, J. Jankovic, Z. Hu, H. Jia and Y. S. Kim, *Nat. Energy*, 2022, **7**, 248-259.
38. S. Yu, L. Xiao and B. C. Benicewicz, *Fuel Cells*, 2008, **8**, 165-174.
39. T. J. Schmidt and J. Baurmeister, *ECS Trans*, 2006, **3**, 861.
40. J. Yang, Q. Li, L. N. Cleemann, C. Xu, J. O. Jensen, C. Pan, N. J. Bjerrum and R. He, *J. Mater. Chem.*, 2012, **22**, 11185-11195.
41. J. S. Yang, L. N. Cleemann, T. Steenberg, C. Terkelsen, Q. F. Li, J. O. Jensen, H. A. Hjuler, N. J. Bjerrum and R. H. He, *Fuel Cells*, 2014, **14**, 7-15.
42. J. Yang, Q. Li, L. N. Cleemann, J. O. Jensen, C. Pan, N. J. Bjerrum and R. He, *Adv. Energy Mater.*, 2013, **3**, 622-630.
43. D. Aili, L. N. Cleemann, Q. Li, J. O. Jensen, E. Christensen and N. J. Bjerrum, *J. Mater. Chem.*, 2012, **22**, 5444-5453.
44. S. Galbiati, A. Baricci, A. Casalegno and R. Marchesi, *Int. J. Hydrog. Energy*, 2013, **38**, 6469-6480.
45. M. S. Kondratenko, I. I. Ponomarev, M. O. Gallyamov, D. Y. Razorenov, Y. A. Volkova, E. P. Kharitonova and A. R. Khokhlov, *Beilstein J. Nanotechnol.*, 2013, **4**, 481-492.

46. A. D. Modestov, M. R. Tarasevich, V. Y. Filimonov and N. M. Zagudaeva, *Electrochim. Acta*, 2009, **54**, 7121-7127.
47. M. A. Molleo, X. Chen, H. J. Ploehn, K. J. Fishel and B. C. Benicewicz, *Fuel Cells*, 2014, **14**, 16-25.
48. Y. Oono, A. Sounai and M. Hori, *J. Power Sources*, 2012, **210**, 366-373.
49. Y. Oono, A. Sounai and M. Hori, *J. Power Sources*, 2013, **241**, 87-93.
50. C. Hartnig and T. J. Schmidt, *J. Power Sources*, 2011, **196**, 5564-5572.
51. J. A. Mader and B. C. Benicewicz, *Macromolecules*, 2010, **43**, 6706-6715.
52. J. Peng, S. Wang, X. Fu, J. Luo, L. Wang and X. Peng, *Adv. Funct. Mater.*, 2023, **33**, 2212464.
53. Q. Zhang, S. Dong, P. Shao, Y. Zhu, Z. Mu, D. Sheng, T. Zhang, X. Jiang, R. Shao, Z. Ren, J. Xie, X. Feng and B. Wang, *Science*, 2022, **378**, 181-186.
54. F. Chen, S. Chen, A. Wang, M. Wang, L. Guo and Z. Wei, *Nat. Catal.*, 2023, **6**, 392-401.
55. P. Guan, Y. Zou, M. Zhang, W. Zhong, J. Xu, J. Lei, H. Ding, W. Feng, F. Liu and Y. Zhang, *Sci. Adv.*, 2023, **9**, eadh1386.